Direct growth of graphene on quartz substrates for label-free detection of adenosine triphosphate

2014 Nanotechnology 25 165702

(http://iopscience.iop.org/0957-4484/25/16/165702)

IOP Publishing Nanotechnology
Nanotechnology **25** (2014) 165702 (10pp) doi:10.1088/0957-4484/25/16/165702

Direct growth of graphene on quartz substrates for label-free detection of adenosine triphosphate

Shicai Xu, Baoyuan Man, Shouzhen Jiang, Weiwei Yue, Cheng Yang, Mei Liu, Chuansong Chen and Chao Zhang

College of Physics and Electronics, Shandong Normal University, Jinan 250014, People's Republic of China

E-mail: byman@sdnu.edu.cn

Received 22 December 2013, revised 8 February 2014
Accepted for publication 26 February 2014
Published 26 March 2014

Abstract

We demonstrate that continuous, uniform graphene films can be directly synthesized on quartz substrates using a two-temperature-zone chemical vapor deposition system and that their layers can be controlled by adjusting the precursor partial pressure. Raman spectroscopy and transmission electron microscopy confirm the formation of monolayer graphene with a grain size of ∼100 nm. Hall measurements show a room-temperature carrier mobility above 1500 $cm^2\ V^{-1}\ s^{-1}$. The optical transmittance and conductance of the graphene films are comparable to those of transferred metal-catalyzed graphene. The method avoids the complicated and skilled post-growth transfer process and allows the graphene to be directly incorporated into a fully functional biosensor for label-free detection of adenosine triphosphate (ATP). This device shows a fast response time of a few milliseconds and achieves a high sensitivity to ATP molecules over a very wide range from 0.002 to 5 mM.

Keywords: graphene, two-temperature zone, chemical vapor deposition, ATP

S Online supplementary data available from stacks.iop.org/Nano/25/165702/mmedia

(Some figures may appear in colour only in the online journal)

1. Introduction

Graphene is a single atomic layer of sp^2 bonded carbon atoms arranged in a two-dimensional hexagonal lattice. It has attracted extensive scientific interest as a result of its distinctive band structure and physical properties [1]. Charge carriers in graphene move at an ultrafast speeds, similar to relativistic, massless Dirac particles, making graphene possess an outstanding conductivity [2–4]. Due to its atom-thick nature, the electrical properties of graphene are highly sensitive to interactions between the graphene surface and adsorbed foreign molecules [5]. By taking advantage of this unique electrochemical property, graphene has recently emerged as a novel nanoelectronic biosensor in the recognition of proteins [6], phenol [7], and single-stranded deoxyribonucleic acid (DNA) [8]. In these cases, the biological detectors were prepared by using mechanically exfoliated graphene or reduced graphene oxide, and their electrical properties were significantly affected by the preparation conditions as a result of the small size of these graphene sheets [9]. In contrast, large-area graphene films grown by chemical vapor deposition (CVD) are more favorable for device fabrication [10]. However, almost all the CVD methods reported to date rely on metal catalysts. Therefore, complicated and skilled transfer techniques have to be employed to transfer the graphene to the dielectric substrates that are required for use in practical electronic devices. During this progress, breakages, organic contamination and metal etching residues are inevitably introduced into the graphene, significantly degrading the performance of graphene-based devices [11]. Therefore, it is essential to develop a practical technique to grow graphene directly on the required substrates. Recently, much work has been done

to explore the catalyst-free growth of graphene on SiO_2 [12], Al_2O_3 [13], MgO [14] and BN [15] by means of conventional CVD technology. Although the directly synthesized graphene films exhibit a nanocrystalline structure with a high level of defects, these efforts have greatly encouraged new attempts to grow graphene directly on the required substrates.

Here we describe a two-temperature-zone CVD method for the direct synthesis of high-quality graphene on quartz substrates. Continuous graphene films were directly grown in the low-temperature zone at 800 °C, and their layers could be controlled by adjusting the flow rate of the precursor gas. The directly synthesized graphene films are of high quality, which can be comparable to metal-catalyzed CVD graphene. Based on this graphene, we fabricated a field-effect transistor (FET) biosensor for label-free detection of ATP molecules. As a universal energy currency, ATP plays an important role in regulating many biological functions in various cells [16]. In particular, it serves as a neurotransmitter or neuromodulator in both the central and peripheral nervous systems [17]. Due to its high conductivity and very clean surface, this graphene-based biosensor achieves a high temporal resolution of a few milliseconds and a high sensitivity to ATP molecules over a very wide range from 0.002 to 5 mM. This technique provides a novel platform to detect ATP molecules and could potentially be employed in studying various essential cellular functions in living cells.

2. Experiment

2.1. Graphene synthesis

Commercially available pure quartz substrates were used in the two-temperature-zone CVD system for graphene growth. All the quartz substrates were first cleaned by sonication in acetone and deionized water. After cleaning, the substrates were placed directly in the low-temperature zone for graphene synthesis. During growth, the high-temperature zone and the low-temperature zone were maintained at 1100 and 800 °C, respectively. A series of pyrometers were used to monitor the temperature distribution in the chamber. After the vacuum reached 1×10^{-6} Torr, the vacuum pumps were closed and the gas mixture of methane (CH_4) and hydrogen (H_2) was introduced into the reaction chamber. Methane was used as a carbon source with a flow rate of 8–400 sccm and hydrogen was controlled to maintain a constant flow of 100 sccm. The typical growth time for graphene is 60 min. After growth, the samples were cooled at a rate of 100 °C min^{-1} under hydrogen flow.

2.2. Characterizations

The morphological changes of quartz substrates were characterized by atomic force microscopy (AFM, Park XE-100) in the noncontact mode. The transmission electron microscopy (TEM) imaging was performed with a transmission electron microscope system (JEOL JEM-2100) operated at 200 kV. For TEM analysis, the samples were first supported with a thin layer of poly (methyl methacrylate) (PMMA) and then immersed in 35% HF solution to separate the graphene from quartz substrates. After rinsing, the thin films were transferred to Cu grids, followed by removal of the polymer by acetone. The thickness and uniformity of the graphene films were evaluated using a Raman Spectrometer (Horiba HR-800) with laser excitation at 532 nm (2.33 eV). A low power of ~1 mW was set to avoid heating or damage to the sample. X-ray photoelectron spectroscopy (XPS) was carried out on a VG ESCA Lab-250 using Al Kα x-rays as the excitation source. Curve fitting of the spectra was carried out using a Lorentzian peak shape. The transmittance of the films was measured using a spectrophotometer (Hitachi U-4000), with a bare quartz substrate as a reference. The electric properties of the graphene films were acquired at room temperature using a Hall effect measurement tool (Accent HL5500). The samples were 6 mm × 6 mm in size, and metal electrodes were made with Ni/Au (10 nm/100 nm) using a conventional van der Pauw contact geometry.

2.3. Preparation of graphene-based biosensor

For device fabrication, source and drain electrodes were prepared across the graphene by spreading a 1 mm thick conductive silver paint (PELCO). A piece of Ni foil (25 μm) as the gate electrode was mounted vertically on the top of the device using silicone rubber (Dow-Corning). Silicone rubber was also used as the dielectric to insulate the electrodes and define the chamber $1.0 \times 1.0 \times 0.2$ cm^3 for recording. The transfer properties of the device were measured using a semiconductor device analyzer (Keithley, Model 4200-SCS).

3. Results and discussion

3.1. Graphene synthesis

The CVD reactor used in this work is illustrated in figure 1. The furnace was designed with two temperature zones in which the temperature can be controlled independently. For the growth, the reactor was set with one zone at 800 °C and the other at 1100 °C. Hydrogen with a flow rate of 100 sccm and methane with a flow rate of 8–400 sccm were introduced into the reactor. In the low-temperature zone, graphene films were formed on the quartz substrates. It was observed that if the methane flow was lower than 10 sccm then no graphene was grown, while if the methane flow was higher than 300 sccm then many defects started to form (figure S1 available at stacks.iop.org/Nano/25/165702/mmedia). The methane flow also affected the growth patterns of graphene. At a low methane flow rate of ~35 sccm, the Raman spectra of all samples show a typical feature of monolayer graphene with a 2D peak intensity approximately twice that of the G peak, even for 180 min growth (figure S2(a) available at stacks.iop.org/Nano/25/165702/mmedia). The monolayer structure can also be confirmed by the TEM image from a folded edge with one dark line in figure S2(b) (available at stacks.iop.org/Nano/25/165702/mmedia). These results indicate that graphene growth on quartz is self-limited at a low methane flow rate. At a higher methane flow rate of ~120 sccm, the graphene layers can be controlled by prolonging the growth time. For the samples grown for 60, 120 and 180 min, the graphene was single layer, double layer and multilayer, respectively (figure S3 available at stacks.iop.org/

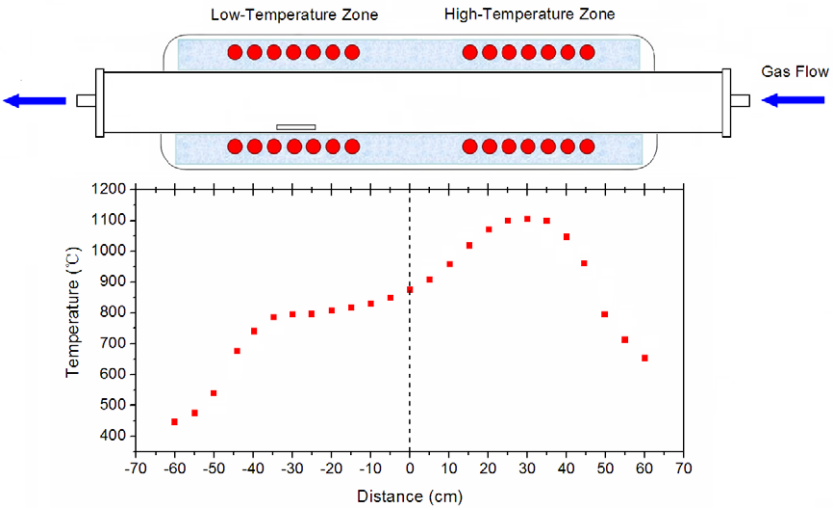

Figure 1. Schematic of the two-temperature-zone CVD system for the growth of graphene on quartz substrates. The temperature distribution in the chamber was recorded by a series of pyrometers.

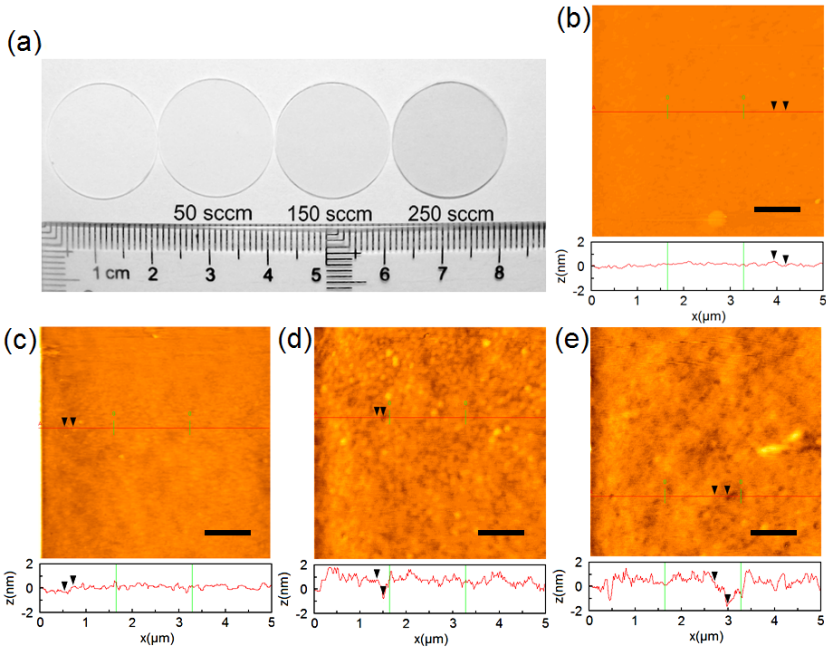

Figure 2. (a) Photographs of the bare quartz substrate and graphene films grown on quartz substrates with different methane flow rates from 50 to 250 sccm. (b) AFM image of the initial surface of the bare quartz substrate. (c)–(e) AFM images of graphene grown for 60 min at methane flow rates of 50, 150 and 250 sccm, respectively. Scale bars, 1 μm.

Nano/25/165702/mmedia). The lowest methane flow rate was optimal to obtain higher quality graphene as long as the condition allowed the formation of graphene. The high-temperature zone was found to be crucial in the growth of graphene by providing enough energy to decompose methane efficiently.

3.2. Characterizations of graphene

Figure 2(a) shows optical photographs of the bare quartz substrate and graphene films grown on quartz substrates with different methane flow rates from 50 to 250 sccm. The transparency of the graphene films decreases significantly with increasing methane flow rate, indicating that the film thickness can be controlled by adjusting the amount of precursor gas. The detailed morphological changes of graphene on quartz substrates are observed by AFM in figures 2(b)–(e). Figure 2(b) shows the image of the initial quartz substrate, which displays a well-polished surface. After exposure to the flowing reaction gas for 60 min, nanoscale corrugations are observed (figures 2(c)–(e)), indicating that graphene has been grown on the quartz substrates. The step height from the height profile roughly indicates the number of layers of graphene [18]. For the samples grown with methane flow rates of 50, 150 and 250 sccm, the AFM images respectively show step heights of

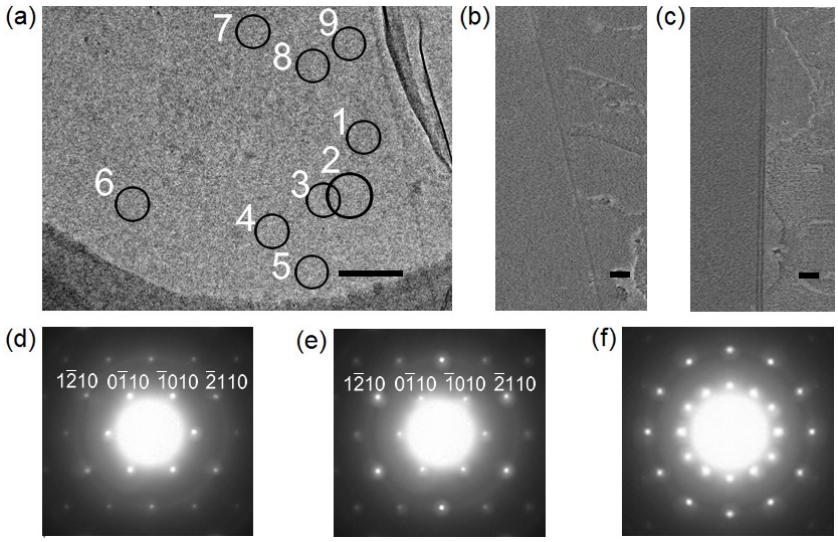

Figure 3. TEM analyses of graphene films produced by using a two-temperature-zone CVD system. (a) Bright-field TEM image of graphene films grown at a flow-rate ratio of $CH_4/H_2 = 50{:}100$ sccm. Scale bar, 200 nm. (b) and (c) TEM images of folded edges for monolayer and bilayer graphene, respectively. Scale bars, 2 nm. (d) and (e) SAED patterns with the peaks labeled by Miller–Bravais indices from the positions of circles 1 and 3, respectively. (f) SAED patterns at the grain boundaries.

~0.4, ~1 and ~2 nm, corresponding to one, three and six layers, respectively [19, 20]. These results agree well with the Raman spectra. As shown in figure S1 (available at stacks.iop.org/Nano/25/165702/mmedia), when the methane flow rate is in the range 10–50 sccm, intensity I_{2D} is approximately twice that of I_G, corresponding to monolayer graphene, and when the methane flow rate is in the range 150–400 sccm, intensity I_{2D} is higher than I_G, indicating multilayer graphene [21].

The crystalline structure of the graphene film was investigated using TEM by transferring it to a small holey copper grid. Figure 3(a) shows the bright-field TEM image of the graphene film grown with a flow-rate ratio of $CH_4/H_2 = 50/100$ sccm. The films are found to be flat and continuous and can be suspended on the grid, indicative of good mechanical properties. To confirm the exact number of layers in the samples, we observed their folded regions by using an electron beam parallel to them. The folded regions exhibit one or two dark lines (figures 3(b) and (c)), suggesting monolayer or bilayer graphene, respectively [22]. Typical patterns with six-fold symmetry are observed by selected-area electron diffraction (SAED) from the region marked with the circle 1 (figure 3(d)). However, we notice that if the electron beam is moved over a distance of a few nanometers or if the beam spot is larger than ~100 nm, two sets of diffraction patterns like those in figure 3(f) are observed. The presence of this diffraction pattern implies that the beam just covers the grain boundaries [23, 24]. This fact suggests that the grain size is about 100 nm. More selected SAED patterns were studied at various positions on the graphene sheets for the sample (figure S4 available at stacks.iop.org/Nano/25/165702/mmedia). Most SAED patterns show typical hexagonally symmetrical patterns with a ratio of $I_{\{1100\}}/I_{\{2110\}} > 1$ (figure 3(d)), with only a few patterns displaying a ratio of $I_{\{1100\}}/I_{\{2110\}} < 1$ (figure 3(e)), demonstrating that a monolayer structure is predominant in this sample [25].

The film thickness and crystalline quality were further evaluated by optical microscopy and Raman spectroscopy. Figure 4(a) shows an optical micrograph of the graphene film with a size of $25 \times 25\ \mu m^2$. The Raman spectra collected from the regions marked with the corresponding colored circles are shown in figure 4(b). The D, G and 2D bands, respectively located at ~1350, ~1590 and ~2700 cm^{-1}, are clearly seen for all samples. The D band is due to the out-of-plane breathing mode of the sp^2 atoms and only gets activated in the presence of the defects. The G band is caused by the first-order scattering of the in-plane optical phonon E_{2g} mode, and the 2D band is the result of a second-order process involving two phonons with opposite momentum [26]. The presence of G and 2D bands is regarded as the signature of graphene, and is quite different from the spectra of the amorphous carbon. The latter has very broad bands enveloping the G and D bands, and the 2D band is absent [27, 28]. The Raman spectrum randomly collected from the lightest background (red circle) in figure 4(a) shows some typical features of monolayer graphene: (i) the intensity ratio $I_{2D}/I_G \geq 2$ and (ii) a single Lorentzian 2D band with a full-width at half-maximum of 35–40 cm^{-1} [29]. The darker flakes (green circle) correspond to bilayer graphene, and the darkest one (blue circle) represents multilayer graphene. Figures 4(c) and (d) show intensity ratios of I_{2D}/I_G and I_D/I_G over the same area as in figure 4(a). The excitation laser spot is about 0.5 μm, and Raman data were obtained at every 0.5 μm. These maps show the uniformity of this material, and the average values of I_{2D}/I_G and I_D/I_G are ~2.1 and ~0.20, respectively. These features indicate that the directly grown graphene is high quality and is comparable to transferred metal-catalyzed graphene. Due to the intensity ratio of I_D/I_G being inversely proportional to the grain size, the quality of graphene and the degree of disorder can be estimated on the basis of the formula $La(nm) = 2.4 \times 10^{-10} \times \lambda^4 \times (I_D/I_G)^{-1}$ [30, 31]. In our

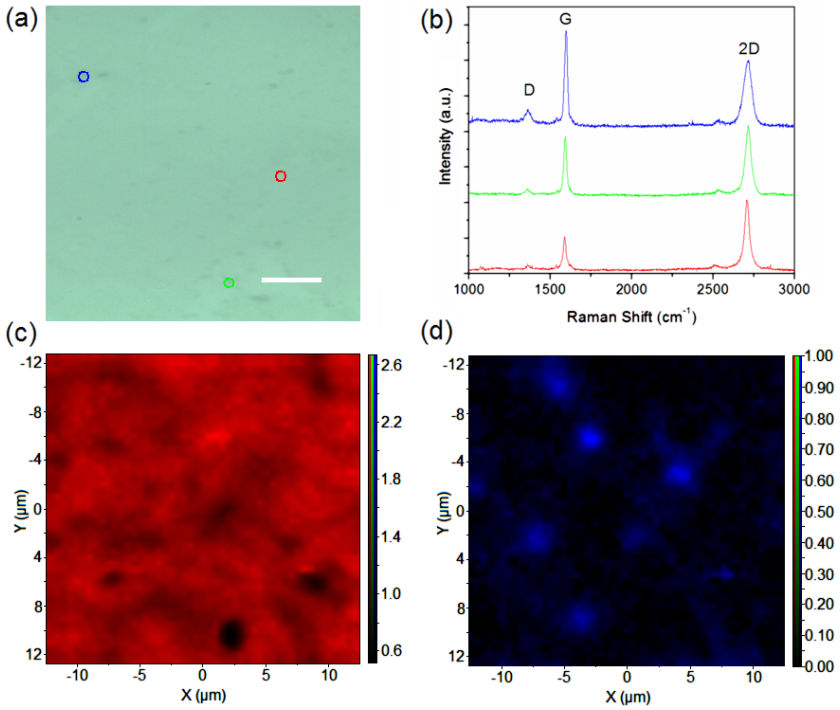

Figure 4. Optical microscopy and micro-Raman spectroscopy images. (a) Optical microscopy image of graphene grown with 50 sccm CH_4 and 100 sccm H_2. Scale bars, 5 μm. (b) Raman spectra from the regions marked with the corresponding colored circles, showing the presence of monolayer, bilayer and multilayer graphene. (c) and (d) Raman maps for intensity ratios of I_{2D}/I_G (c) and I_D/I_G (d) over the same region as in (a).

case, the wavelength λ of the excitation laser is 532 nm and the I_D/I_G ratio is ∼0.20. The grain size of this material is estimated to be ∼96 nm, which is consistent with the graphene grain size of ∼100 nm determined by TEM. The Raman spectra corresponding to bilayer graphene and multilayer graphene are also observed from the sample exposed to the higher flow rate of methane, as shown in figures S1 and S3 (available at stacks.iop.org/Nano/25/165702/mmedia). In comparison with transferred metal-catalyzed CVD graphene on SiO_2, the G and 2D bands show a remarkable blueshift, which may derive from the strong compressive strain effect of the quartz substrate formed in the graphene growth process [32].

XPS measurement shows the typical characteristic peak of graphene for the sample grown with 50 sccm methane (figure 5(a)). It can be deconvolved into two components. The main peak at 284.4 eV indicates the formation of a sp^2 C–C network for the grown film [33]. The discernible tail at 285.6 eV is assigned to the hydroxyl carbon C–O [34]. The XPS spectrum of the graphene film grown with a higher methane flow rate is shown in figure S5 (available at stacks.iop.org/Nano/25/165702/mmedia), where the intensity of the C–O bond is obviously higher than that of the film formed with a lower methane flow rate of 50 sccm. It is probably due to amorphous carbon contamination being more easily formed in a higher methane flow rate. The signals related to Cu, Fe, Co, Ni, or other metals are not observed in the full XPS spectrum (figure S6 available at stacks.iop.org/Nano/25/165702/mmedia), confirming that no metal impurities were introduced during the graphene growth process and graphene can be grown on quartz without a metal catalyst. Figure 5(b) shows transmission spectra of graphene grown on quartz substrates with different methane flow rates. The graphene shows a high transmittance in the visible and near-IR regions. At a wavelength of 550 nm, the transmittance of our thinnest graphene film is ∼97%, a value similar to that of monolayer graphene [35]. The transmittance decreases significantly with increasing flow rate of methane as more layers of graphene can be formed at a higher methane concentration. For the samples formed at the higher methane flow rate of 350 sccm, the transmittance drops to ∼82% at 550 nm. Figure 5(c) compares the sheet resistance of our work with those of other studies as a function of transmittance at 550 nm. A sheet resistance of ∼270 Ω $\square^{-1}$ with a transmittance of ∼82% is obtained in our case. The value is one to two orders of magnitude lower than those of well-reduced graphene oxide or graphene oxide [36, 37], and can be comparable to those of metal-catalyzed CVD graphene [35, 38, 39]. The carrier mobility and carrier concentration of the graphene films were obtained by Hall effect measurements at room temperature in the ambient atmosphere using a conventional van der Pauw contact geometry. Figure 5(d) shows that the mobility of graphene is in the range 500–1520 $cm^2\ V^{-1}\ s^{-1}$ with a carrier concentration of 3.7×10^{12}–2.4×10^{13} cm^{-2}. The relation between mobility and carrier concentration can be categorized by different methane flow rates. The graphene film grown with the lowest methane flow rate has the highest carrier mobility. As noted in figure S1 (available at stacks.iop.org/Nano/25/165702/mmedia), graphene grown with lower methane flow rates tends to have better structural quality and thus less charge carrier scattering in this film. In all cases the material

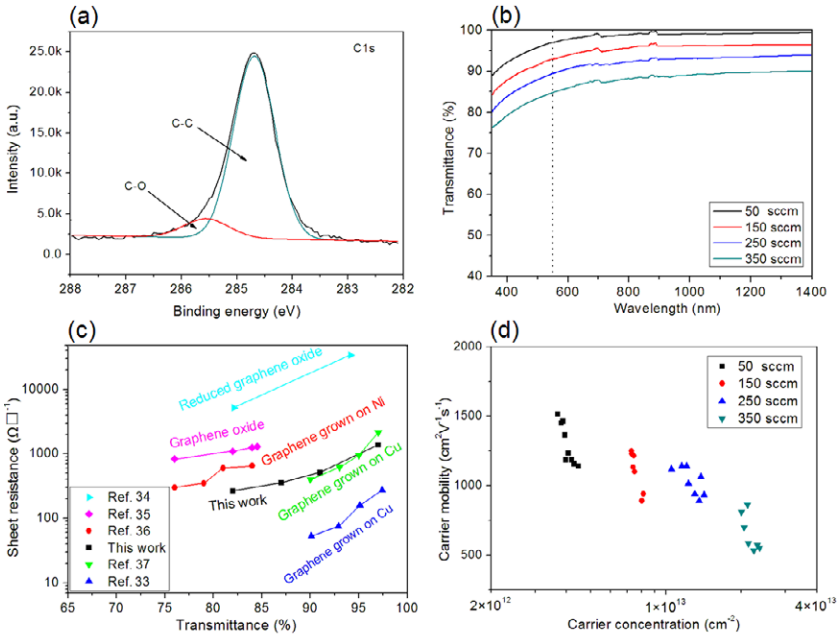

Figure 5. (a) XPS spectrum of the graphene film grown on quartz substrate with 50 sccm methane. (b) UV–vis spectra of graphene films grown with methane flow rates of 50, 150, 250 and 350 sccm, respectively. (c) Comparison of the resistance and transmittance of the graphene films obtained in this work and other examples in the literature. (d) Relationship between mobility and carrier concentration for the graphene films grown with different methane flow rates.

exhibits p-type characteristics. The high carrier mobility is greater than those obtained using oxygen-aided synthesis on SiO_2 ($\mu = 531$ cm^2 V^{-1} s^{-1}) [12], remote catalyzation on silica ($\mu = 600$ cm^2 V^{-1} s^{-1}) [33], and also compare favorably with that of Cu-catalyzed small-grain graphene ($\mu = 1200$ cm^2 V^{-1} s^{-1}) from Kim *et al* [40]. The excellent optical and electrical properties can be attributed to the direct growth process, as it avoids the complex transfer process with its associated problems of film breakage and contamination.

3.3. Discussion of the graphene growth mechanism

For a long time, CVD of non-catalytic graphene on quartz substrates has been considered impossible, or at least very difficult. To get a thorough understanding of the growth model, the early stage of graphene growth was monitored by AFM. The growth process was controlled by introducing a low flow rate of methane (15 sccm) along with hydrogen (100 sccm). After 15 min growth, the whole system was cooled immediately. Many flake-like features with sizes from 20 to 100 nm are observed (figure 6(a)). These flakes can be interpreted as the nucleation sites of graphene. The height profile AA′ across the flakes reveal a step height of 3–4 Å, which agrees well with the thickness of monolayer graphene [18–20]. Figure 6(b) shows the AFM image of the enlarged graphene nuclei after 30 min growth. These nuclei grow to 100–300 nm, but their thickness remains at a height of 3–4 Å (profile BB′), displaying a typical two-dimensional growth model. If we assume that the average-sized nucleation seed in figure 6(a) grew and became one of the average-sized grains in figure 6(b), then the lateral growth rate would be ∼9.3 nm min^{-1}. The subsequent process follows this growth pattern, as demonstrated by the image of the complete graphene film after 60 min growth, whose height profile CC′ shows a step height of ∼4 Å, corresponding to monolayer graphene (figure 6(c)) [18–20]. The two-dimensional growth is possible by considering the fact that the cohesion energy between quartz and graphene is higher than that between graphene and graphene [13, 41]. Therefore, the subsequent carbon species tend to land on the bare quartz substrate instead of stacking on top of these graphene domains, displaying a self-limited growth process. However, with increasing methane flow rate, more carbon species were formed and thus gave more opportunities for carbon adsorption, resulting in bilayer or multilayer graphene.

In this work, we found that graphene film can be grown directly on quartz substrates in the low-temperature zone but did not grow in the high-temperature zone in a moderate precursor concentration. To provide more insight into the mechanism, a contrast experiment was set up with the low-temperature zone working alone. However, we failed to find that graphene can grow in this case. This result suggests that the high-temperature zone plays an important role in growing graphene, although the graphene cannot grow in the high-temperature zone itself. Thermal dissociation of methane can be described as $CH_4 = C + 2H_2$ ($\Delta H = 75.6$ kJ mol^{-1}) [42]. This reaction occurs readily at 1100 °C without a metal catalyst [12, 13]. Therefore, in the high-temperature zone, the methane can be broken down, generating large numbers of carbon species, including CH_x ($x < 4$) fragments, carbon monomers and carbon dimers. As illustrated on the right side of figure 6(d), these carbon species were active and tended to be adsorbed on the substrate by C–O and H–O binding [12, 43], but at the same time the high-energy thermal vibrations force the carbon species to leave the substrate [13], making stable

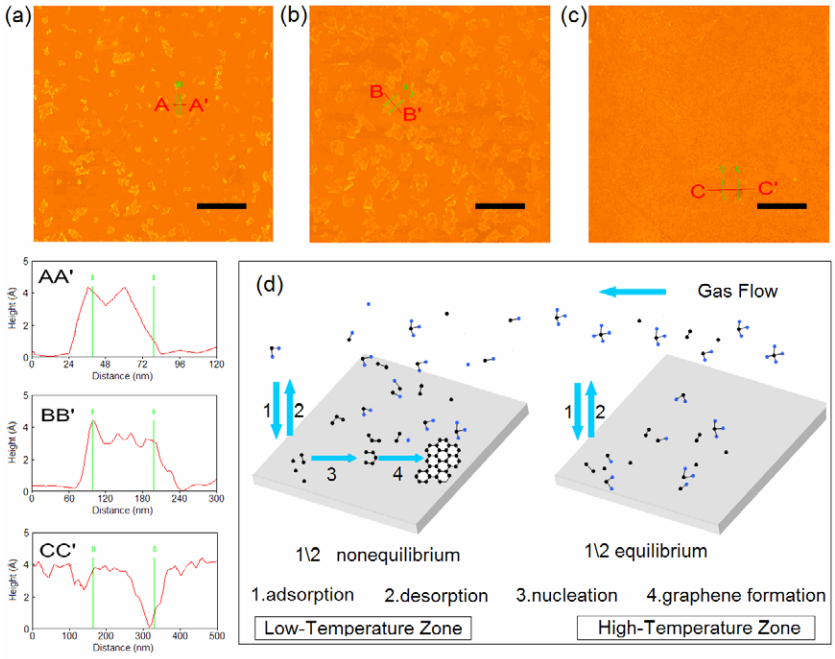

Figure 6. Graphene growth process recorded by AFM for (a) 15 min, (b) 30 min and (c) 60 min. Scale bars, 500 nm. (d) Schematic of graphene nucleation and the growth mechanism on quartz substrates. In the high-temperature zone, carbon atoms are supplied by the decomposition of methane, balanced by high-energy thermal vibrations. In the low-temperature zone, a fraction of carbon adatoms can survive high-energy thermal vibrations and evolve to form graphene nuclei.

graphene nuclei hard to form. However, as illustrated on the left side of figure 6(d), when these carbon species fly into the low-temperature zone with the gas flow, where the thermal vibrations are relatively mild, some carbon species can fortuitously stay on the substrates, forming the initial nucleus by C–C coupling. The subsequent carbon species begin to make bonds to them, landing on the edge of the stable nuclei. Finally, these nuclei coalesce to form a continuous film, fully covering the substrate surface. For the contrast experiment, when we just use the low-temperature zone, methane cannot decompose efficiently at the low temperature of 800 °C and the carbon species have difficulty forming bonds with the substrate to form stable nuclei due to their lower activation. Therefore, the temperature differences between the two zones just create a condition where the high-temperature zone offers enough power to crack methane and the low-temperature zone slows down the thermal vibrations to promote nucleation and initiate the growth of graphene.

In fact, graphene growth is still possible in the high-temperature zone if a high precursor concentration is employed, but with a high level of defects (Raman spectrum in figure S7 available at stacks.iop.org/Nano/25/165702/mmedia). This high-temperature phenomenon can be attributed to the formation of large carbon flakes at high precursor concentrations that can sustain high-energy thermal vibrations and evolve into graphene nuclei [13]. In our work, graphene films grown in the low-temperature zone are relatively high quality, most probably because a high H_2/CH_4 flow-rate ratio was used. Active atomic hydrogen can decrease the growth rate, promote the growth of large graphene grains and lead to high-quality graphene [44]. Moreover, according to studies on the role of kinetic factors in graphene growth on Cu, when the mass transport coefficients (hg) $\gg$ surface reaction constants (Ks), one expects to form uniform graphene [45]. So, in our case, the high quality of graphene may also be attributed to the relatively low growth rate of ~9.3 nm min^{-1}. The high quality and clean surface of this direct-grown graphene make it an ideal candidate for bioprobes used in biosensors.

3.4. Graphene biosensor and its performance

Figure 7(a) shows the schematic of a biosensor using directly grown graphene as a bioprobe. The devices were directly fabricated on the graphene/quartz substrate in the configuration of an FET. The source, drain and gate electrodes are insulated by silicone rubber, defining a chamber of size $1.0 \times 1.0 \times 0.2$ cm^3 for recording. Before detection, ATP molecules were dissolved to different concentrations in the range from 0.002 to 10 mM in ddH_2O (double distilled water). Figure 7(b) shows the transfer properties of the graphene-based FET operated with ddH_2O in the chamber. The charge neutrality point appears very close to the zero-gate voltage, and its conductance is sensitive to voltage gating and therefore desirable for electrical biosensing. Figure 7(c) shows the variation of drain–source current (I_{ds}) passing through the graphene as the test samples were introduced into the recording chamber. Many upward current spikes were detected on the introduction of ATP aqueous solution (0.002–10 mM) at a gate voltage of 0.7 V. In order to further understand the response characteristics, a single current spike is depicted on an expanded timescale. The current spike exhibits two distinct kinetic phases: a rapidly rising phase on a timescale of a few milliseconds and a

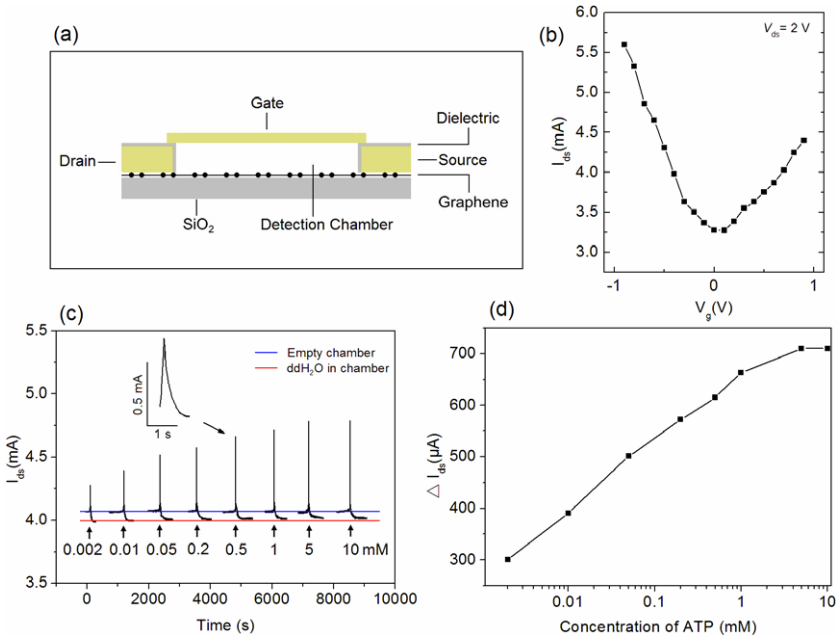

Figure 7. (a) Structural schematic of the graphene biosensor. (b) Transfer curves of the graphene biosensor operated with ddH_2O in the chamber at $V_{ds} = 2$ V. (c) Responses of the graphene biosensor to ATP aqueous solution concentrations from 0.002 to 10 mM. The inset is the single current spike depicted on an expanded timescale. The straight red line indicates a I_{ds} level of ∼4 mA, when the device operates with the ddH_2O in chamber. The straight blue line indicates a I_{ds} level of ∼4.1 mA, when device works with the chamber empty. Graphene-based FET operated at $V_{ds} = 2$ V, and $V_g = 0.7$ V. (d) Change of drain–source current (ΔI_{ds}) with the concentration of ATP molecules.

long-lasting decaying phase on a timescale of a few hundred milliseconds. The rapid response phase likely corresponds to the dynamic processes of the release of ATP molecules onto the surface of graphene after its introduction. Because ATP molecules are negatively charged, they will increase the hole concentration and thus reduce the resistance of graphene as they are trapped on the graphene surface. The decay in the current signal is presumably due to the escape process of ATP molecules from the graphene surface, because negatively charged ATP molecules tend to move upwards under the positive electric field. As all the ATP molecules rise from the graphene surface, the current (I_{ds}) decreases to the same level as the device operated with ddH_2O in the chamber (red straight line). After each measurement, the device was successively cleaned in acetone, deionized water and ddH_2O and dried in a vacuum oven. After these cleaning and drying steps, the current (I_{ds}) recovered its original level of ∼4.1 mA, when the device is operated with the chamber empty (the blue straight line). The graphene-based biosensor also shows a high specificity in ATP detection. The spiky responses were never observed when graphene was immersed in a solution that contains ions, proteins, secreted molecules or other molecules. These molecules in the solution only affect the base-line current of the graphene-based device (figure S8 available at stacks.iop.org/Nano/25/165702/mmedia). In fact, unlike most molecules in solution, the ATP molecules are able to directly interact with graphene through adenine nucleobases, similar to the nucleobases of DNA binding to carbon nanotube sidewalls via the pi–pi stacking interaction [46, 47]. This close contact exerts a strong influence on the graphene conductance and thus renders a measurable current response. Figure 7(d) shows the change of the drain–source current (ΔI_{ds}) as a function of the concentration of ATP molecules. It is found that ΔI_{ds} increases roughly linearly with the logarithm of ATP concentration over a very wide range from 0.002 to 5 mM. This range covers almost all the concentrations in actual internal environments of living bodies. This fact indicates that the graphene biosensor is suitable for the detection of ATP. When the ATP concentration is above 5 mM, the amplitude of the transient current signal tends to saturate. It is possible that at this concentration all the adsorption sites on the graphene have been filled by ATP molecules. Therefore, the remaining ATP molecules are not able to interact directly with graphene or further affect its conductance. The sensor sensitivity can be defined by sensitivity $= \Delta I_{ds}/I_{ds0} \times 100\%$, where I_{ds0} is the drain–source current in ddH_2O. The sensor shows a more than 50% increase of current to an exposure to 5 mM ATP. Even for a much lower ATP concentration of 0.002 mM, there is also an obvious signal with a corresponding current increase of 23%. This high sensitivity can be understood from the atom-thick nature of graphene. The atom-thick nature makes the electrical properties of graphene highly sensitive to adsorbed foreign molecules [5].

4. Conclusions

We have developed a two-temperature-zone CVD process for synthesizing continuous, uniform graphene films on quartz substrates without a metal catalyst. Graphene films can be grown directly on quartz substrates, making their surface free from residual metal impurities or polymer contamination. The optical transmittance and conductance of these

graphene films are comparable to those of transferred metal-catalyzed graphene. Based on this graphene film, we fabricated a graphene biosensor in the configuration of an FET for label-free detection of ATP molecules. This graphene-based nanoelectronic device shows a high temporal resolution of a millisecond and gives a high sensitivity to ATP molecules over a very wide range from 0.002 to 5 mM. Meanwhile, this report provides the possibility to study dynamic biological processes in living cells by detecting ATP release.

Acknowledgments

This work was financially supported by the National Natural Science Foundation of China (11274204 and 61205174), Shandong Excellent Young Scientist Research Award Fund (BS2012CL034), Shandong Province Higher Educational Science and Technology Program (J12LA07) and Graduate Innovation Fund (BCX1203).

References

[1] Novoselov K S, Geim A K, Morozov S V, Jiang D, Katsnelson M I, Grigorieva I V and Dubonos S V 2005 Two-dimensional gas of massless Dirac fermions in graphene *Nature* **438** 197–200

[2] Nair R R, Blake P, Grigorenko A N, Novoselov K S, Booth T J, Stauber T, Peres N M R and Geim A K 2008 Fine structure constant defines visual transparency of graphene *Science* **320** 1308

[3] Flores M Z S, Autreto P A S, Legoas S B and Galvao D S 2009 Graphene to graphane: a theoretical study *Nanotechnology* **20** 465704

[4] Lu G, Ocola L E and Chen J 2009 Reduced graphene oxide for room-temperature gas sensors *Nanotechnology* **20** 445502

[5] Chen T Y, Loan P T K, Hsu C L, Lee Y H, Wang J T W, Wei K H, Lin C T and Li L J 2013 Label-free detection of DNA hybridization using transistors based on CVD grown graphene *Biosens. Bioelectron.* **41** 103–9

[6] Ohno Y, Maehashi K, Yamashiro Y and Matsumoto K 2009 Electrolyte-gated graphene field-effect transistors for detecting pH and protein adsorption *Nano Lett.* **9** 3318–22

[7] Liu F, Piao Y, Choi K S and Seo T S 2012 Fabrication of free-standing graphene composite films as electrochemical biosensors *Carbon* **50** 123–33

[8] Tang Z, Wu H, Cort J R, Buchko G W, Zhang Y, Shao Y, Aksay I A, Liu J and Lin Y 2010 Constraint of DNA on functionalized graphene improves its biostability and specificity *Small* **6** 1205–9

[9] Su C Y, Xu Y, Zhang W, Zhao J, Tang X, Tsai C H and Li L J 2009 Electrical and spectroscopic characterizations of ultra-large reduced graphene oxide monolayers *Chem. Mater.* **21** 5674–80

[10] Chen C H, Lin C T, Lee Y H, Liu K K, Su C Y, Zhang W and Li L J 2012 Electrical probing of submicroliter liquid using graphene strip transistors built on a nanopipette *Small* **8** 43–6

[11] Wang Y, Tong S W, Xu X F, Özyilmaz B and Loh K P 2011 Interface engineering of layer-by-layer stacked graphene anodes for high-performance organic solar cells *Adv. Mater.* **23** 1514–8

[12] Chen J Y, Wen Y G, Guo Y L, Wu B, Huang L P, Xue Y Z, Geng D C, Wang D, Yu G and Liu Y Q 2011 Oxygen-aided synthesis of polycrystalline graphene on silicon dioxide substrates *J. Am. Chem. Soc.* **133** 17548–51

[13] Sun J, Cole M T, Lindvall N, Teo K B K and Yurgens A 2012 Noncatalytic chemical vapor deposition of graphene on high-temperature substrates for transparent electrodes *Appl. Phys. Lett.* **100** 022102

[14] Rümmeli M H, Bachmatiuk A, Scott A, Börrnert F, Warner J H, Hoffman V, Lin J H, Cuniberti G and Büchner B 2010 Direct low-temperature nanographene CVD synthesis over a dielectric insulator *ACS Nano* **7** 4206–10

[15] Ding X L, Ding G Q, Xie X M, Huang F Q and Jiang M H 2011 Direct growth of few layer graphene on hexagonal boron nitride by chemical vapor deposition *Carbon* **49** 2522–5

[16] Fields R D and Stevens B 2000 ATP: an extracellular signaling molecule between neurons and glia *Trends Neurosci.* **23** 625–33

[17] Gourine A V, Llaudet E, Dale N and Spyer K M 2005 ATP is a mediator of chemosensory transduction in the central nervous system *Nature* **436** 108–11

[18] Novoselov K S, Geim A K, Morozov S V, Jiang D, Zhang Y, Dubonos S V, Grigorieva I V and Firsov A A 2004 Electric field effect in atomically thin carbon films *Science* **306** 666–9

[19] Lee S, Lee K and Zhong Z H 2010 Wafer scale homogeneous bilayer graphene films by chemical vapor deposition *Nano Lett.* **10** 4702–7

[20] Reina A, Jia X T, Ho J, Nezich D, Son H B, Bulovic V, Dresselhaus M S and Kong J 2009 Large area, few-layer graphene films on arbitrary substrates by chemical vapor deposition *Nano Lett.* **9** 30–5

[21] Dong X, Wang P, Fang W, Su C Y, Chen Y H, Li L J, Huang W and Chen P 2011 Growth of large-sized graphene thin-films by liquid precursor-based chemical vapor deposition under atmospheric pressure *Carbon* **49** 3672–8

[22] Meyer J C, Geim A K, Katsnelson M I, Novoselov K S, Booth T J and Roth S 2007 The structure of suspended graphene sheets *Nature* **446** 60–3

[23] Kim K, Lee Z, Regan W, Kisielowski C, Crommie M F and Zettl A 2011 Grain boundary mapping in polycrystalline graphene *ACS Nano* **5** 2142–6

[24] Liu N, Fu L, Dai B, Yan K, Liu X and Zhao R Q 2011 Universal segregation growth approach to wafer-size graphene from non-noble metals *Nano Lett.* **11** 297–303

[25] Hernandez Y *et al* 2008 High-yield production of graphene by liquid-phase exfoliation of graphite *Nature Nanotechnol.* **3** 563–8

[26] Ferrari A C *et al* 2006 Raman spectrum of graphene and graphene layers *Phys. Rev. Lett.* **97** 187401

[27] Tamor M A and Vassell W C 1994 Raman 'fingerprinting' of amorphous carbon films *J. Appl. Phys.* **76** 3823–30

[28] Schwan J, Ulrich S, Batori V, Ehrhardt H and Silva S R P 1996 Raman spectroscopy on amorphous carbon films *J. Appl. Phys.* **80** 440–8

[29] Li X S *et al* 2009 Large-area synthesis of high-quality and uniform graphene films on copper foils *Science* **324** 1312–4

[30] Cançado L G, Takai K, Enoki T, Endo M, Kim Y A, Mizusaki H, Jorio A, Coelho L N, Paniago R M and Pimenta M A 2006 General equation for the determination of the crystallite size l_a of nanographite by Raman spectroscopy *Appl. Phys. Lett.* **88** 163106

[31] Hwang J *et al* 2013 van der Waals epitaxial growth of graphene on sapphire by chemical vapor deposition without a metal catalyst *ACS Nano* **7** 385–95

[32] Cheng Z, Zhou Q, Wang C, Li Q, Wang C and Fang Y 2011 Toward intrinsic graphene surfaces: a systematic study on thermal annealing and wet-chemical treatment of SiO_2-supported graphene devices *Nano Lett.* **11** 767–71

[33] Teng P Y, Lu C C, Hasegawa K A, Lin Y C, Yeh C H, Suenaga K and Chiu P W 2012 Remote catalyzation for direct formation of graphene layers on oxides *Nano Lett.* **12** 1379–84

[34] Tien H W, Huang Y L, Yang S Y, Wang J Y and Ma C C M 2011 The production of graphene nanosheets decorated with silver nanoparticles for use in transparent, conductive films *Carbon* **49** 1550–60

[35] Bae S *et al* 2010 Roll-to-roll production of 30-inch graphene films for transparent electrodes *Nature Nanotechnol.* **5** 574–8

[36] Becerril H A, Mao J, Liu Z F, Stoltenberg R M, Bao Z N and Chen Y S 2008 Evaluation of solution-processed reduced graphene oxide films as transparent conductors *ACS Nano* **2** 463–70

[37] Zhao J P, Pei S F, Ren W C, Gao L B and Cheng H M 2010 Efficient preparation of large-area graphene oxide sheets for transparent conductive films *ACS Nano* **4** 5245–52

[38] Kim K S, Zhao Y, Jang H, Lee S Y, Kim J M, Kim K S, Ahn J H, Kim P, Choi J Y and Hong B H 2009 Large-scale pattern growth of graphene films for stretchable transparent electrodes *Nature* **457** 706–10

[39] Li X S, Zhu Y W, Cai W W, Borysiak M, Han B Y, Chen D, Piner R D, Colombo L and Ruoff R S 2009 Transfer of large-area graphene films for high-performance transparent conductive electrodes *Nano Lett.* **9** 4359–63

[40] Kim E, Yu T H, Song E S and Yu B 2011 Chemical vapor deposition-assembled graphene field-effect transistor on hexagonal boron nitride *Appl. Phys. Lett.* **98** 262103

[41] Koenig S P, Boddeti N G, Dunn M L and Bunch J S 2011 Ultrastrong adhesion of graphene membranes *Nature Nanotechnol.* **6** 543–6

[42] Kozlov G I and Knorre V G 1962 Single-pulse shock tube studies on the kinetics of the thermal decomposition of methane *Combust. Flame* **6** 253–63

[43] Liu B *et al* 2011 Importance of oxygen in the metal-free catalytic growth of single-walled carbon nanotubes from SiO_x by a vapor–solid–solid mechanism *J. Am. Chem. Soc.* **133** 197–9

[44] Gao L *et al* 2012 Repeated growth and bubbling transfer of graphene with millimetre-size single-crystal grains using platinum *Nature Commun.* **3** 699–705

[45] Bhaviripudi S, Jia X, Dresselhaus M S and Kong J 2010 Role of kinetic factors in chemical vapor deposition synthesis of uniform large area graphene using copper catalyst *Nano Lett.* **10** 4128–33

[46] Huang Y, Sudibya H G, Fu D, Xue R, Dong X, Li L J and Chen P 2009 Label-free detection of ATP release from living astrocytes with high temporal resolution using carbon nanotube network *Biosens. Bioelectron.* **24** 2716–20

[47] Johnson R R, Johnson A T C and Klein M L 2008 Probing the structure of DNA—carbon nanotube hybrids with molecular dynamics *Nano Lett.* **8** 69–75